

Characterisation of interface friction strain-rate dependency of soft sediments at low stresses using a ring penetrometer

VIKRAM SINGH*, HENNING MOHR*, SAM STANIER†, BRITTA BIENEN* and MARK F. RANDOLPH*

The ring penetrometer is a shallow rotational penetrometer that has been developed to characterise the mechanical behaviour of surficial marine sediments. The strain-rate dependency of soils is crucial to the design of a wide range of offshore geotechnical infrastructure founded in the upper layers of the seabed (e.g. pipelines, cables and shallow foundations). This paper explores the potential application of a ring penetrometer test to measure the strain-rate dependency of the interface friction generated in soft soils at low stresses. Large-deformation numerical models of the test are developed using an elastoplastic constitutive model and a viscoplastic variant with strain softening. Using parameters representative of kaolin clay and a calcareous silt from an offshore location, the numerical analyses demonstrate a clear and measurable influence of both the viscous and strain-softening behaviours on the device–soil interface friction. These simulations were used to design suitable experimental protocols for multi-rate ring penetrometer tests, the results of which yielded a strain-rate dependency of 9–16% and 22–26% per log cycle in the kaolin clay and calcareous silt, respectively, which compare favourably with measurements derived from T-bar twitch experiments. Finally, models are presented that can be applied in the interpretation of varying-rate ring penetrometer test data for application in practice.

KEYWORDS: laboratory tests; large-deformation finite-element modelling; offshore engineering; numerical modelling; ring penetrometer testing; soft seabed characterisation; strain-rate effects; strain softening and hardening

INTRODUCTION

The characterisation of surficial fine-grained sediments, such as the silts and clays typically found in deeper waters offshore, requires devices and test protocols capable of measuring properties at low effective stresses of the order of 5–20 kPa. Conventional in situ penetrometer testing methods, such as cone and full flow penetrometers (i.e. T-bar and ball penetrometer) can be applied to measure the strength profile of the shallow sediments (White *et al.*, 2010). However, such tests provide no insight into the frictional properties of the interface between objects such as pipelines or cables and the underlying soil.

The remote intelligent geotechnical seabed surveys joint industry project (RIGSS JIP), which was conducted at the University of Western Australia (UWA), developed a selection of shallow penetrometer devices which have been used in the laboratory and in practice offshore to characterise shallow seabed sediments (see Yan *et al.*, 2011; Yan, 2013; Stanier & White, 2015; Randolph *et al.*, 2018; Schneider *et al.*, 2019, 2020a, 2020b). Application of the various types of shallow penetrometer devices, including shapes such as a toroid and a hemiball, has also been extensively explored using numerical modelling approaches (Yan *et al.*, 2011; Randolph *et al.*, 2012; Yan, 2013; Schneider *et al.*, 2019, 2020b). In these studies, simple constitutive models (i.e. Tresca and modified Cam Clay (MCC)) were adopted in order to develop models to aid the interpretation of experimental data, resulting in the measurement of properties for use in design in compliance with current

industry guidelines (e.g. DNV-GL-FP114 (DNV, 2017)). To date, these interpretation techniques have focused on the transition from undrained to drained behaviour at relatively modest sliding rates, and with the accumulation of small deformations, such that the friction mobilised tends to rise with increasing rotation from an undrained limit to a drained limit (Schneider *et al.*, 2020b). However, the undrained strength of fine-grained sediments is well known to increase by 5–15% per log cycle of increasing shear strain rate, and some offshore infrastructure such as sliding foundations (Cocjin *et al.*, 2014) and on-bottom pipelines (Randolph *et al.*, 2012) undergo rapid undrained movements encapsulating a wide range of strain rates in this ‘viscous’ range.

This paper explores the potential for measuring the near-surface strain-rate dependency of the frictional characteristics of fine-grained soils at low stresses using a ring penetrometer by way of a combination of numerical and physical modelling techniques. The ring penetrometer is a type of shallow penetrometer testing device that has been developed to characterise the mechanical behaviour of surficial soft soils. It is similar in concept to the toroid penetrometer described by Schneider *et al.* (2020b), but with more direct interpretation techniques due to the surface of the device being flat, meaning that no ‘wedging’ correction is required, which also provides a direct measure of interface friction that is comparable with interface shear box tests – the current ‘de facto’ standard for interface friction measurement. First, large-deformation finite-element (LDFE) analyses of a ring penetrometer test have been performed using a classical MCC-based elastoplastic constitutive model (Mašin, 2009) and a viscoplastic variant incorporating strain-softening and strain-hardening features (Singh *et al.*, 2022). The numerical results demonstrate that the ring penetrometer could be used to measure strain-rate dependency and the simulation results were subsequently used to design suitable experimental test protocols and interpretation methods. The interface friction response is characterised by the so-called ‘backbone’ curves in

Manuscript received 19 February 2022; revised manuscript accepted 26 September 2022.

Discussion on this paper is welcomed by the editor.

* Centre for Offshore Foundation Systems, University of Western Australia, Perth, WA, Australia.

† Cambridge University Engineering Department, University of Cambridge, Cambridge, UK.

both time and strain-rate space that have been fitted to the simulation results using simple equations. In the second part of this paper, an experimental programme has been carried out comprising both ring penetrometer and T-bar penetrometer tests performed on two different fine-grained soils, namely kaolin clay and a calcareous silt from an offshore location. Strain-rate effects obtained from the ring and T-bar tests are compared in order to validate application of the ring penetrometer test as a means of determining the viscous properties of shallow surficial deposits, which is particularly useful in the analysis of pipeline-seabed and cable-seabed interactions.

THEORY – RING PENETROMETER

A typical ring penetrometer test involves three phases: (a) a penetration phase targeting the shear strength (s_u); (b) a dissipation phase aimed at the consolidation properties (c_v); and (c) a rotation phase targeting the undrained, transition and drained interface friction properties by rotating at different rotation speeds (μ_u , μ' or δ , $T_{r,50}$).

Consolidation coefficient from dissipation stage

During the initial penetration, the ring is loaded to a target vertical load. After reaching the target vertical load, the vertical load is immediately halved to limit ring settlement during the dissipation and rotation stages and kept constant to allow consolidation. Based on the measured excess pore pressure, the coefficient of consolidation (c_v) can be estimated using the following relationship

$$c_v = \frac{T_{50} D_{\text{ring}}^2}{t_{50}} \quad (1)$$

where t_{50} is the time required for dissipation of 50% of the generated excess pore pressures and T_{50} is a non-dimensional time factor for 50% dissipation. The T_{50} values for a ring penetrometer are typically derived using LDFE analyses. In order to identify the c_v value, an optimisation of the c_v value is performed that matches the experimental data best at time t_{50} .

Interface strength parameters from rotation stage

During the rotation stage, the average normal stress induced on the ring penetrometer–soil interface σ_n due to the vertical load V maintained on the penetrometer from the dissipation stage can be expressed as

$$\sigma_n = \frac{V}{A_c} \quad (2)$$

where A_c is the contact surface area between the ring penetrometer and the soil as illustrated in Fig. 1. The contact area A_c is given by

$$A_c = 2\pi r_{\text{eff}} D_{\text{ring}} \quad (3)$$

where r_{eff} is the effective radius and D_{ring} is the width of the cross-section of the device (see Fig. 1). The effective normal stress acting on the penetrometer–soil interface is estimated by removing the contribution of the measured excess pore pressures u_{excess} from the total stress acting on the surface of the ring penetrometer and is calculated as

$$\sigma'_n = \sigma_n - \beta u_{\text{excess}} \quad (4)$$

where β is a scaling factor to account for the position of pore pressure transducers. The pore pressure transducers are located at the invert of the device, and the values measured by them represent an overestimation of the average pore

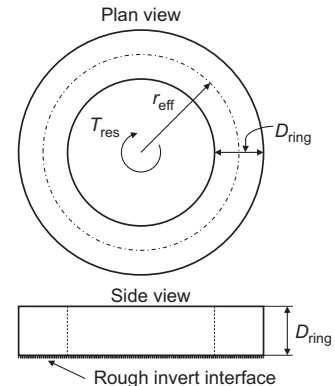


Fig. 1. Schematic representation of a ring penetrometer

pressure acting on the contact surface area between the ring penetrometer and the soil. The scaling factor, β , therefore, allows the correct average pore pressure to be obtained at the base of the device. The β values were derived from finite-element solutions by performing an analysis of penetration stage of the ring test and taking the ratio of average pore pressure at the device base and the pore pressure developed at the centre of the cross-section. During the rotation stage, the measured torsional resistance T_{res} can be converted to an equivalent axial force F as follows

$$F = \frac{T_{\text{res}}}{r_{\text{eff}}} \quad (5)$$

Thus, the interface shear stress can be expressed as

$$\tau = \frac{F}{A_c} \quad (6)$$

This facilitates the derivation of total and effective stress friction factors μ and μ' from τ and σ_n or σ'_n , given, respectively, by

$$\mu = \frac{\tau}{\sigma_n} = \frac{T_{\text{res}}}{V r_{\text{eff}}} \quad (7)$$

$$\mu' = \frac{\tau}{\sigma'_n} = \frac{T_{\text{res}}}{(V - \beta u_{\text{excess}} A_c) r_{\text{eff}}} \quad (8)$$

The quantity μ is similar to the friction factor measured in an interface shear box test and quantity μ' is equivalent to $\tan(\delta)$, where δ is the effective friction angle of the soil.

NUMERICAL MODELLING OF RING PENETROMETER TEST

Large-deformation finite-element analyses of the ring penetrometer test have been performed using the commercial finite-element software Abaqus with rate-independent structured modified Cam Clay (SMCC) (Mašín, 2009) and a rate-dependent version – namely, the viscoplastic recoverable sensitivity (VRS) constitutive model (Singh *et al.*, 2022). The model parameters selected were calibrated for UWA kaolin clay. First, the analyses involving undrained penetration of the ring, dissipation of the generated excess pore pressure and subsequent rotation of the ring with several rotation rates were carried out using the classical MCC model form of the SMCC model (i.e. no strain-softening and strain-rate effects) to highlight the importance of considering strain-softening in such analyses. Second, the analyses were repeated using the VRS model to explore the effects of softening and rate dependency on the inferred interface friction characteristics.

FE modelling details

The LDDE analyses of the ring test have been developed using the remeshing and interpolation technique with small strains (RITSS) strategy (Hu & Randolph, 1998) in Abaqus, where an LDDE analysis is split into several small-strain finite-element analyses to avoid mesh distortion. A new mesh is generated at the end of every small-strain simulation, and the soil state (i.e. stresses, state and field variables) are then mapped from the old deformed mesh to the new mesh. In this paper, displacement-controlled effective stress analysis with pore pressure was carried out to achieve an undrained ring penetration of $0.1D_{\text{ring}}$ in ten RITSS steps, following which a load-controlled consolidation analysis, with a vertical maintained stress equivalent to half of the maximum undrained penetration resistance achieved, was performed in a single RITSS step. Similarly, the rotation stage simulation was completed post-consolidation in a single small-strain three-dimensional (3D) analysis.

The ring penetrometer shown in Fig. 1 has been modelled as a rigid part with a completely rough interface at the base. The ‘completely rough interface’ referred to here is an interface condition where the interface friction angle is equal to the effective friction angle of soil, meaning that the interface friction mobilised upon slippage is equal to the shear strength of the soil on the interface. Owing to axial symmetry, a two-dimensional (2D) axisymmetric ring–soil domain has been adopted for the penetration and dissipation stages (see Fig. 2(a)), while a 3D sliced domain has been created for the rotation stage in order to take advantage of the cyclic symmetry of the problem (see Fig. 2(b)). The horizontal and vertical extents of the soil part were considered as $20D_{\text{ring}}$ radius and $20D_{\text{ring}}$ height, sufficient to avoid any boundary effects, and a 5° slice was used to create the mesh for rotation stage. Basic finite-element modelling checks were performed in order to assess any influence of far-field boundaries (i.e. $20D_{\text{ring}}$ radius and $20D_{\text{ring}}$ height) on penetrometer response in the simulations, of which there was none for modest variations in far-field boundary distance. These checks were mainly related to the observation of any changes in the soil state and field variables in far-field locations due to penetrometer loading. For the 2D and 3D domain discretisations, eight-node biquadratic displacement, bilinear pore pressure, reduced integration elements (CAX8RP in the Abaqus standard library) and 20-node triquadratic displacement, trilinear pore pressure, reduced integration (C3D20RP in the Abaqus standard library) were used, respectively. A fully drained boundary condition was prescribed at the top surface of the model, except at the soil part in direct contact with the ring, allowing dissipation of the excess pore pressures. To create a non-zero mudline strength, a surcharge pressure of 10 kPa was applied at the free surface of the soil, which results in a mudline strength of about 2 kPa. At the end of the dissipation stage, the soil state was mapped from the axisymmetric mesh to the 3D slice mesh, allowing all three stages of the ring test to be modelled in a linked series of analyses.

Constitutive model

The soil response in the ring analyses has been described using the SMCC and VRS constitutive models. The implementation of the SMCC (Mašin, 2009) and VRS models (Singh *et al.*, 2022) in LDDE analyses has been detailed in Singh *et al.* (2021) and Singh *et al.* (2022). Only a brief overview is given here.

The SMCC model requires nine material parameters: (a) the basic parameters M , λ^* , κ^* , N^* and G (or v); and (b) the strain-softening parameters k , A , S_t and S_f . The basic parameters have physical interpretations that are identical to the classical MCC model parameters, except that the

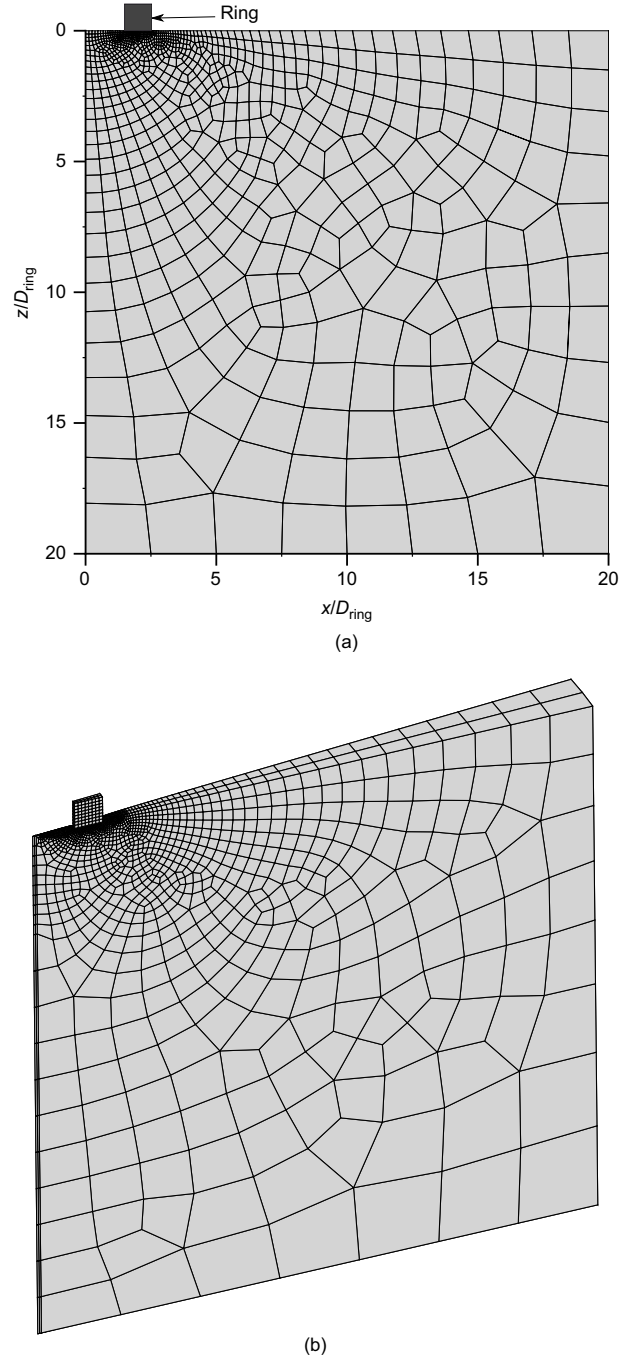


Fig. 2. Typical finite-element mesh adopted for: (a) penetration and dissipation stages; (b) rotation stage

so-called Butterfield compression law (Butterfield, 1979) has been used. On loading and unloading of compressible soils, the Butterfield compression law gives a more realistic linear relationship between $\ln(1+e)-\ln p'$ than with the conventional $e-\ln p'$ form, simplifying the assignment of the compression and swelling parameters (i.e. slopes of normal compression line (NCL), λ^* and unload-reload line (URL), κ^*). The second set of parameters – the softening rate k , relative contribution of plastic volumetric and deviatoric strains ratio A , true soil sensitivity S_t and final (at fully remoulded state) soil sensitivity S_f – control the softening response. The model has two state variables: void ratio e and sensitivity s_{ep} . The yield surface (f) is given by

$$f = q^2 + M^2 p' (p' - s_{\text{ep}} p_c) \quad (9)$$

where p' and q are the mean effective stress and deviatoric stress, respectively. The initial and final values of the sensitivity state variable s_{epi} and s_{epf} can be derived from the slopes of the NCL, λ^* , and URL, κ^* , and the initial and final sensitivities, S_t and S_f , respectively, by

$$s_{\text{epi}} = S_t^{[\lambda^*/(\lambda^* - \kappa^*)]} \quad (10)$$

$$s_{\text{epf}} = S_f^{[\lambda^*/(\lambda^* - \kappa^*)]} \quad (11)$$

Assuming associated flow results in a plastic potential surface that is identical to the yield surface as given by equation (9). The void ratio e is related to the quantity p_c , which is the size of the yield surface for $s_{\text{ep}} = 1$, through

$$\ln(1+e) = N^* - \kappa^* \ln p' - (\lambda^* - \kappa^*) \ln \left(\frac{p_c}{p_r} \right) \quad (12)$$

where p_r is a reference pressure, taken as 1 kPa. The soil response is elastic inside the yield surface and is controlled by the shear modulus G and bulk modulus K . Any stress states on the yield surface induce plastic deformation, which degrades the soil sensitivity state variable as per the following equation

$$\dot{s}_{\text{ep}} = -\frac{k}{(\lambda^* - \kappa^*)} (s_{\text{ep}} - s_{\text{epf}}) \dot{\varepsilon}_s \quad (13)$$

$\dot{\varepsilon}_s$ is the equivalent plastic strain rate controlling the softening response, given by

$$\dot{\varepsilon}_s = \sqrt{(1-A)(\dot{\varepsilon}_v^p)^2 + A(\dot{\varepsilon}_q^p)^2} \quad (14)$$

where $\dot{\varepsilon}_v^p$ and $\dot{\varepsilon}_q^p$ are the plastic volumetric and deviatoric strain rates, respectively. The change in state variable e is driven by incremental volumetric strain rate $\dot{\varepsilon}_v$ according to

$$\dot{e} = -(1+e)\dot{\varepsilon}_v \quad (15)$$

To explore strain-rate effects, a viscoplastic version of the SMCC model based on the Perzyana's overstress theory (Perzyna, 1966) was developed and implemented in Abaqus by Singh *et al.* (2022). In this enhancement, a viscoplastic flow rule based on an overstress function is defined to obtain a relationship between $\dot{\varepsilon}^{\text{vp}}$, current stress state and the size of the yield surface. This was achieved by defining a static yield surface identical in shape and size to the yield surface of the SMCC model f (equation (9)) and a dynamic loading surface f_d passing through the current stress state (Perzyna, 1966), given, respectively, by

$$f = q^2 + M^2 p' (p' - s_{\text{ep}} p_c) = q^2 + M^2 p' (p' - p_{\text{cs}}) \quad (16)$$

$$f_d = q^2 + M^2 p' (p' - p_{\text{cd}}) \quad (17)$$

where the shapes of f and f_d are assumed to be identical but with different sizes, p_{cs} and p_{cd} , respectively. Assuming an associated flow rule with f_d , the viscoplastic strain rate $\dot{\varepsilon}^{\text{vp}}$ is written as

$$\dot{\varepsilon}^{\text{vp}} = \mu_v \langle \phi(F) \rangle \frac{\partial f_d}{\partial \sigma} \quad (18)$$

where μ_v (h^{-1}/kPa) is a fluidity parameter and $\phi(F)$ is an overstress function representing the distance between f and f_d . The Macaulay brackets $\langle \rangle$ are used to define the overstress function such that $\langle \phi(F) \rangle = \phi(F)$ if $F > 0$ and $\langle \phi(F) \rangle = 0$ if $F \leq 0$. This means that the viscoplastic strains occur only when the stress state is outside the static yield

Table 1. SMCC and VRS model parameters for kaolin clay

Model	Parameter	Value
SMCC/VRS	Slope of NCL, λ^*	0·0811
	Slope of URL, κ^*	0·019
	Poisson's ratio, ν	0·3
	Frictional constant, M	0·90
	NCL intercept at $p' = 1$ kPa, N^*	1·195
	Initial sensitivity, S_t	3·08
	Final sensitivity, S_f	1·0
	Degradation rate, k	0·02
	Degradation ratio, A	0·2
	Fluidity parameter, μ_v : h^{-1}/kPa	$3·6 \times 10^{-4}$
VRS	Viscosity exponent, N_v	20·0
	Sensitivity recovery parameter, R	1·0

surface. The overstress function of exponential form (Yin *et al.*, 2006; Yin & Hicher, 2008) is adopted, which can be written as

$$\phi(F) = \left\{ \exp \left[N_v \left(\frac{p_{\text{cd}}}{p_{\text{cs}}} - 1 \right) \right] - 1 \right\} \quad (19)$$

where N_v is a viscosity parameter. The model parameters are identical to those of the SMCC model – that is basic parameters and softening parameters, but three additional parameters are required related to the viscosity μ_v and N_v and sensitivity recovery ratio R . The evolution of the state variable s_{epi} and e are still controlled by the strains, as in equations (13) and (15), with equation (13) modified to include the consolidation induced recovery of s_{ep} controlled by the recovery parameter R . The detailed implementation is available in Singh *et al.* (2022).

Material parameters

The SMCC and VRS model parameters for kaolin clay were adopted from Singh *et al.* (2021) and Singh *et al.* (2022) and are presented in Table 1. The basic parameters of the VRS model were considered identical to the SMCC model and the viscous parameters were selected based on direct simple shear analyses, giving a 7% strength enhancement for each log cycle increase in strain rate in kaolin clay. The non-strain-softening version of the SMCC model was used and the softening parameters for the VRS model were calibrated from a cyclic T-bar test. The parameter R was taken as unity, as previously calibrated from the episodic T-bar penetration test in kaolin clay reported in Singh *et al.* (2022). The permeability and effective unit weight of kaolin clay were considered as 1×10^{-9} m/s and 7·5 kN/m³.

Analysis details

The ring was initially penetrated by $0·1D_{\text{ring}}$ from the mud-line with a penetration velocity v_p of 3 mm/s, giving a normalised velocity $v_p D_{\text{ring}}/c_v > 100$ that is sufficient to maintain undrained conditions. After achieving the target penetration, the ring was unloaded to $0·5V_{\text{max}}$, where V_{max} is the maximum undrained penetration resistance at the final penetration of the ring, in a load-controlled consolidation analysis, maintaining this load until the dissipation of the excess pore pressure was complete. The resulting over-consolidation of soil has minimal impact on viscous effects (Robinson, 2019). Finally, the rotation analyses were carried out to explore the torsional capacity for several values of normalised rotational velocity, $v_r D_{\text{ring}}/c_v$ in the range of 0·01–5000, covering the entire range of drained to fully undrained and viscous regimes.

Numerical results and interpretation models

The numerical results obtained from the ring analyses using the rate-independent SMCC model with no softening are presented in Fig. 3. Fig. 3(a) plots the penetration resistance normalised by intact undrained shear strength and ring thickness ($V/s_{ui}D_{ring}$) against the normalised penetration depth (w/D_{ring}), showing the increase in the resistance with depth. The excess pore pressure dissipation response maintaining half of the penetration resistance at w/D_{ring} of 0.10 as vertical load on the ring is shown in Fig. 3(b), in which average invert excess pore pressure normalised by the initial value of the average excess pore pressure $\bar{u}_{excess}/\bar{u}_{excess-i}$ at the ring base is plotted against dimensionless time T , expressed as

$$T = \frac{c_v t}{D_{ring}^2} \quad (20)$$

where c_v is the coefficient of consolidation and t is the dissipation time. The dissipation response has been fitted using a hyperbolic function (see solid line in Fig. 3(b))

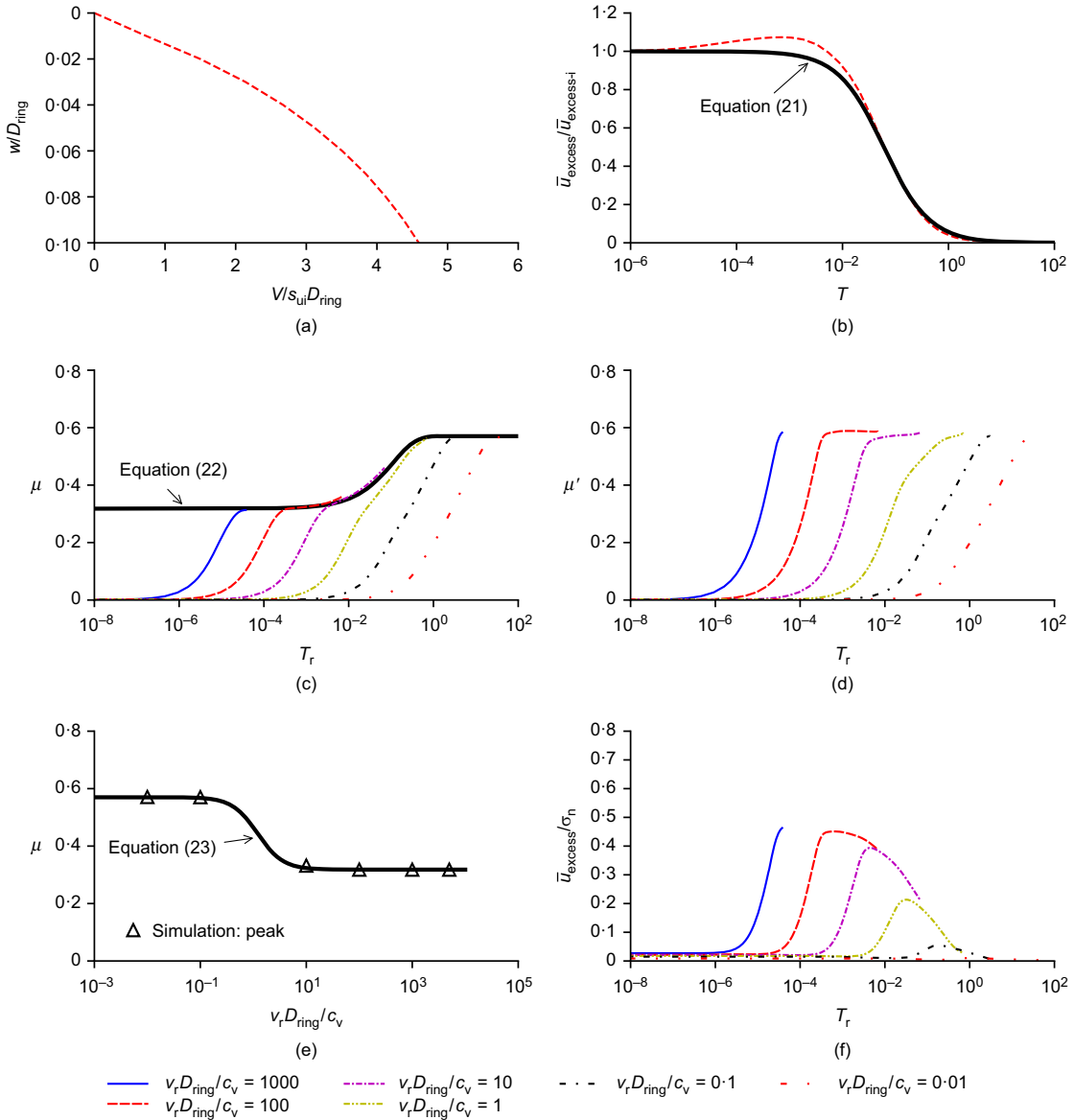


Fig. 3. Numerical results of ring penetrometer analyses using rate-independent non-softening SMCC model: (a) normalised penetration response; (b) normalised excess pore pressure in dissipation stage with dimensionless time; (c) interface friction with dimensionless time; (d) effective friction with dimensionless time; (e) interface friction with dimensionless rotational velocity; and (f) normalised excess pore pressure in rotation stage with dimensionless time

given as follows

$$\frac{\bar{u}_{excess}}{\bar{u}_{excess-i}} = \frac{1}{1 + (T/T_{50})^m} \quad (21)$$

where m is a fitting parameter and T_{50} is a dimensionless time required for 50% dissipation of the excess pore pressure. The total and effective interface friction coefficients (μ and μ' , respectively) obtained from the rotation analyses with $v_r D_{ring}/c_v$ values from 1000 to 0.01 are plotted against dimensionless rotation time T_r in Figs 3(c) and 3(d). Fig. 3(e) plots the mobilised μ values against $v_r D_{ring}/c_v$ and Fig. 3(f) presents the excess pore pressure normalised by total normal stress σ_n against T_r . The faster rotation speeds ($v_r D_{ring}/c_v = 100$ and 1000) lead to undrained shearing of the interface, causing build-up of the excess pore pressure, which results in lower total friction being generated at the interface. These excess pore pressures start dissipating if the shearing continues (see Fig. 3(f)). In contrast, for the slower velocities ($v_r D_{ring}/c_v < 100$), the dissipation of the excess pore pressure during shearing causes higher values of μ and

smaller $\bar{u}_{\text{excess}}/\sigma_n$, with almost drained response for the $v_r D_{\text{ring}}/c_v = 0.1$ and 0.01 cases. The friction factor μ achieves a peak value of 0.32 in the undrained regime and 0.56 in the drained regime. The friction factor mobilised is both rate and time dependent, such that if the undrained rotation rate simulations had been continued indefinitely, they would have reached the same asymptotic friction factor as the drained rotation rate simulations. For the limited magnitude of rotation modelled here, the mobilisation responses for each rotation velocity are different but the peak μ values, as suggested by Randolph *et al.* (2012), can be traced by a single backbone curve given by

$$\mu = \mu_d - (\mu_d - \mu_u)0.5^{(T_r/T_{r,50})^n} \quad (22)$$

where $T_{r,50}$ is the T_r value required for achieving a μ value halfway between μ_u and μ_d and n is a fitting parameter. Here μ_u is the initial peak undrained total friction, which in some instances is less than the drained limit (i.e. μ_d), which is the maximum undrained total friction that could theoretically be mobilised if the device were rotated continuously at an undrained rate. The effective interface friction coefficient μ' achieves an identical value for all the velocities when the peak value has been mobilised (see Fig. 3(d)). The excess pore pressure no longer increases due to non-softening conditions and starts decreasing due to dissipation (see Fig. 3(f)). To capture the consolidation response, using the form of the expression proposed by Chow *et al.* (2020) for full-flow penetrometers, the peak μ values ($\mu_u = 0.32$ and $\mu_d = 0.57$) can be fitted into a normalised velocity backbone curve as shown in Fig. 3(e) and expressed as

$$\mu = \mu_u \left(\frac{\mu_d/\mu_u + (V'/V'_{50})^{\lambda_1}}{1 + (V'/V'_{50})^{\lambda_1}} \right) \quad (23)$$

where $V' = v_r D_{\text{ring}}/c_v$ and V'_{50} is the dimensionless rotational velocity at which the frictional resistance is halfway between undrained and drained extremes. Here, the value of the fitting parameter λ_1 is 1.8 , and $V'_{50} = 1.2$. It is to be noted that these analyses are somewhat idealistic as they do not incorporate strain-rate and softening effects, but have been used previously to illustrate consolidation effects.

The results obtained from the analyses performed using the VRS model are presented in Fig. 4 in an identical format to the rate-independent analyses. Owing to strain-rate dependency, slightly higher values of the penetration resistance, $V/s_{ui} D_{\text{ring}}$, are obtained in comparison to the rate-independent analyses, a peak value of 5.85 against 4.56 (compare Fig. 4(a) with Fig. 3(a)). The pore pressure dissipation response plotted in Fig. 4(b) demonstrates a slightly higher increase in the excess pore pressure at the onset of the dissipation stage due to a ‘Mandel–Cryer’ effect. The reason behind this is the development of additional excess pore pressure due to the sudden decrease in the strain rate at the beginning of the dissipation stage. The results obtained from the rotation stage reveal the influence of the strain softening and strain rate on the μ and μ' . In the viscous regime of the interface shearing, consideration of strain softening causes the friction factor μ to decrease after achieving a peak value (see Fig. 4(c)) due to a further softening-induced increase in the excess pressure as demonstrated in Fig. 4(f). This effect has also been observed in experiments performed with the toroid (Schneider *et al.*, 2020b). As might be expected, the peak values of μ decrease linearly with successive reductions in the normalised velocity, $v_r D_{\text{ring}}/c_v$, due to the development of higher excess pore pressure at slower rotation rates (compare peak μ values for $v_r D_{\text{ring}}/c_v = 5000$ to 50). This is true until the dissipation of the pore pressure begins to dominate the response, leading to

an increase in μ as the rotation becomes partially drained. In contrast, the drained value of the interface friction factors μ_d and μ' are not affected by the viscous effects (due to the lower strain rates occurring at the low rotation rates) and their values are close to those obtained using the rate-independent version of the model. In order to capture both the consolidation and viscous effects in the backbone curves, equations (22) and (23) can be rewritten, respectively, as

$$\mu = \mu_d - (\mu_d - \mu_u \eta)0.5^{(T_r/T_{r,50})^n} \quad (24)$$

$$\mu = \mu_u \eta \left[\frac{\mu_d/\mu_u + (V'/V'_{50})^{\lambda_1}}{1 + (V'/V'_{50})^{\lambda_1}} \right] \quad (25)$$

where η is the strain-rate effect on the undrained friction factor given by

$$\eta = \left\{ \frac{1 + \lambda_2 \times \max [v_r/D_{\text{ring}} / (v_r/D_{\text{ring}})_{\text{ref}}, 1]^{\lambda_3}}{1 + \lambda_2} \right\} \quad (26)$$

Here, the reference nominal strain rate $(v_r/D_{\text{ring}})_{\text{ref}} = 1\%/\text{h}$ is considered to represent the rate-independent analyses, leading to the value of the peak undrained friction factor equal to μ_u . The value of the parameter λ_2 , a viscous property of the soil, depends on the selected value of the $(v_r/D_{\text{ring}})_{\text{ref}}$, and λ_3 is the shear thinning index which typically lies in the range 0.05 – 0.15 (Randolph *et al.*, 2012). The value of the fitting parameter λ_2 is 0.7 , and λ_3 is 0.073 . The fits obtained using equations (24) and (25) are plotted in Figs 4(c) and 4(e). The v_r/D_{ring} value in equation (24), which plots μ against T_r , is calculated using the following equation

$$\frac{v_r}{D_{\text{ring}}} = \frac{\delta_{\text{rp}} / (T_r D_{\text{ring}}^2 / c_v)}{D_{\text{ring}}} \quad (27)$$

where δ_{rp} is the rotational displacement required to mobilise μ_u . The numerical results, if plotted in the form of μ against δ_r (i.e. linear displacement of the ring in rotation stage), reveal that δ_{rp} values for different rotation speeds are similar. It can be seen that equations (24) and (25) fit the numerical results well, allowing both consolidation and viscous effects to be captured in μ plotted against T_r and μ plotted against $v_r D_{\text{ring}}/c_v$ spaces. The summary of all fitting parameters is given in Table 2.

The numerical analyses demonstrate that the ring penetrometer test can be applied to investigate viscous and consolidation dependency of geotechnical design properties of surficial soils, and the simple fitting equations proposed here allow ready adoption of these solutions in practical design applications. One key detail is that performing a suite of experiments with each having a constant rotation rate – as simulated here – would not be sensible in practice due to the potential for local sample variability, which would introduce significant uncertainty into the interpretation. Instead, an experimental protocol ought to be designed to have multiple periodically reducing rotation rates, in order to capture the rate effects in a single test in one footprint. However, this approach could not be modelled numerically due to the cyclic symmetric nature of the simulation of the rotation phase adopted here.

PHYSICAL MODELLING OF RING PENETROMETER TEST IN KAOLIN CLAY AND A CALCAREOUS SILT

An experimental series of ring penetrometer tests was carried out to investigate whether strain-rate effects on soil properties under low stresses could be captured in reality, in

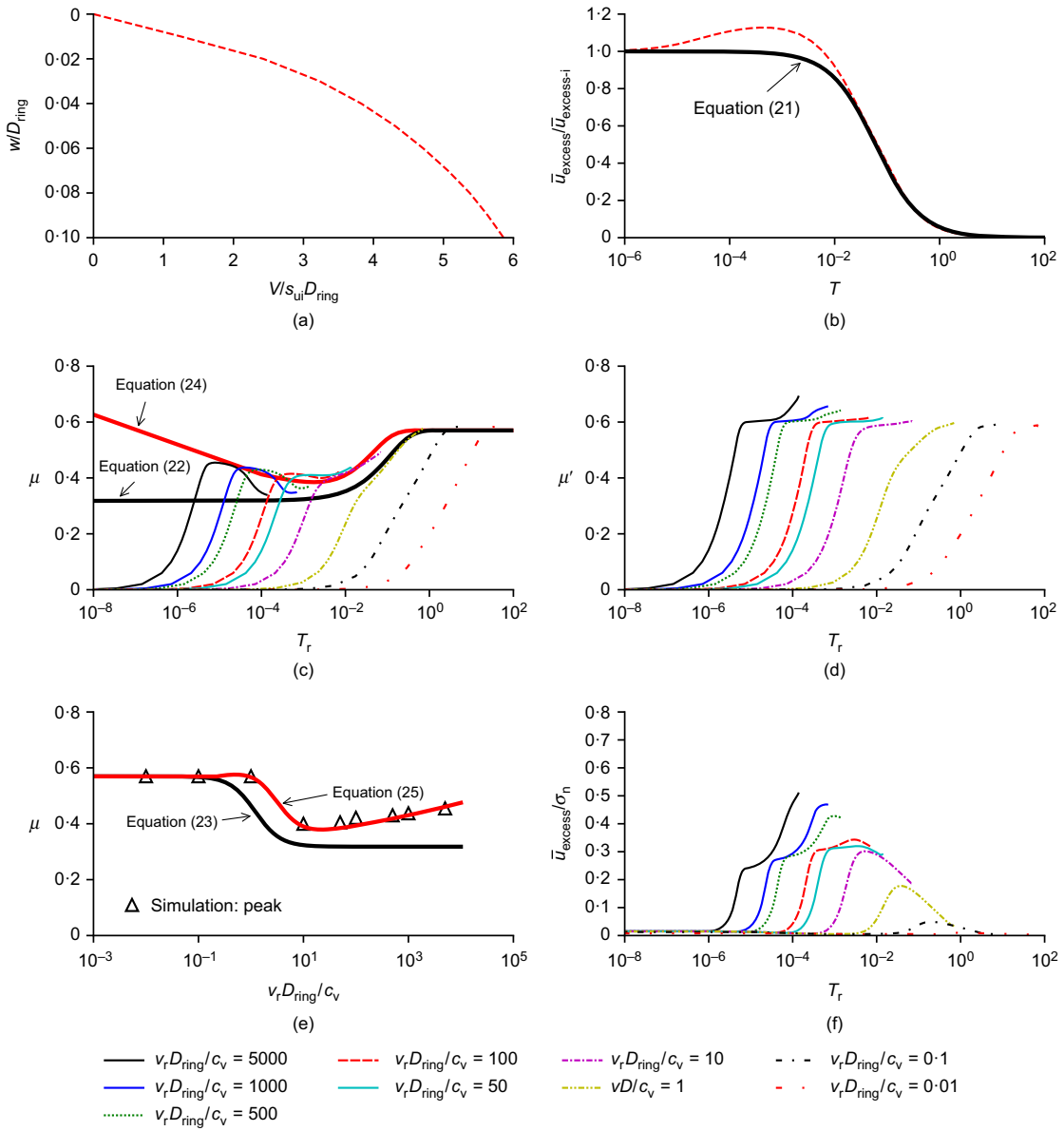


Fig. 4. Numerical results of ring penetrometer analyses using rate-dependent strain-softening VRS model: (a) normalised penetration response; (b) normalised excess pore pressure in dissipation stage with dimensionless time; (c) interface friction with dimensionless time; (d) effective friction with dimensionless time; (e) interface friction with dimensionless rotational velocity; and (f) normalised excess pore pressure in rotation stage with dimensionless time. A full-colour version of this figure can be found on the ICE Virtual Library (www.icevirtuallibrary.com)

Table 2. Summary of the model fitting parameters adopted in the interpretation of the numerical analyses

Parameter	Value
μ_u	0.32
μ_d	0.57
T_{50}	0.06
m	1.0
$T_{r,50}^*$	0.07
$T_{r,50}^\dagger$	0.03
n	0.8
λ_1	1.8
λ_2	0.7
λ_3	0.073
V'_{50}^*	1.2
V'_{50}^\dagger	3.0
$\delta_r: \text{m}$	0.00082

*SMCC.

†VRS.

the same manner as suggested in the preceding numerical work. The ring penetrometer and actuator system is graphically illustrated in Fig. 5. The ring penetrometer used had a cross-section width D_{ring} of 25 mm and a lever arm r_{eff} of 50 mm, giving an overall diameter of 125 mm. The interface of the ring was coated with a coarse silica sand, resulting in a roughness of $R_a \approx 120 \mu\text{m}$, which can be presumed to be fully rough according to Meyer *et al.* (2015). The ring was equipped with a load cell that measured the vertical and torsional load as well as four differential pore-pressure transducers (PPTs) located at the interface of the ring. A more detailed description of the actuation system shown in Fig. 5, which was developed at the UWA, can be found in the paper by Schneider *et al.* (2020a).

The test protocol adopted first involved undrained penetration of the ring to a target vertical load of 100 N. At the end of this initial penetration, the device was unloaded to 50% of its initial load, which was then held constant while the excess pore pressures generated during penetration were allowed to dissipate. At the end of dissipation, the device was rotated at

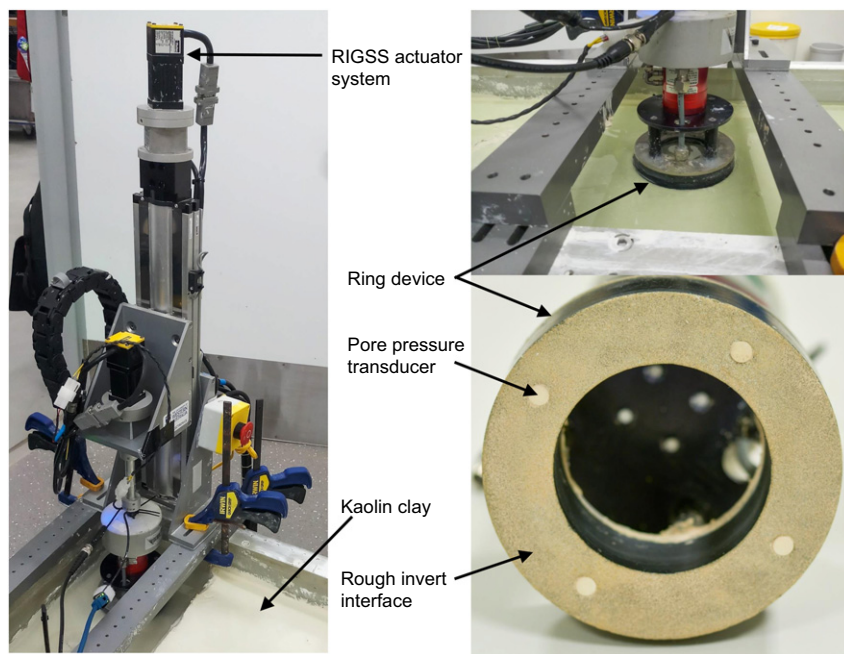


Fig. 5. Experimental set-up for a ring penetrometer test

rates in the range of from 5 to 0.00158/s. The transition between each rate is an instantaneous change in device rotation speed. To allow for any potential lag between rate changes and consequential changes in pore pressure, during the fastest rotation speed, the device was rotated through 30°, ensuring full mobilisation of residual friction and maximising the generation of excess pore pressure. In subsequent stages the rotation applied was reduced to 15°, which limited device settlement while still being sufficient to mobilise the frictional resistance in each stage. In this way, the experiments differ significantly from the simulations summarised in Fig. 4, for example, because it is more economical to perform a multi-rate test in a single footprint in practice.

Two types of soils were used for the testing campaign. The first was a commercially available kaolin clay (Table 3) and the second was a calcareous silt, which was recovered from the North West Shelf of Western Australia using a 225 mm dia. sample tube sub-sampled from a box core recovered to the deck of a survey vessel. This allowed direct testing on a real, largely intact sample using the ring penetrometer. The results from testing the kaolin clay and calcareous silt samples are explained in detail below. A summary of all the test results in both soils is presented at the end, focusing on the strain-rate effects.

Soil preparation and characterisation

The kaolin clay was mixed in a slurry and poured into a strong box of 1.3 m × 0.39 m in plan. It should be mentioned here that in the ring experiments the kaolin was obtained from a different supplier than the kaolin simulated in the numerical analyses. Subsequently the slurry was consolidated in a hydraulic press with step-wise load increments to an undrained strength s_u of approximately 2–3 kPa, which was obtained from cyclic T-bar penetration testing. The final sample height was 150 mm. In this test, a 5 mm dia. (D) T-bar was penetrated into the sample with a velocity v_p of 3 mm/s, giving a normalised velocity $v_p D_{\text{ring}} / c_v = 67$, which is sufficient to ensure undrained conditions (Lehane *et al.*, 2009). The experiments carried out in reconstituted kaolin clay and the intact calcareous silt in the sampling tube are referred to hereafter as ‘intact’ tests. In a second set of

Table 3. Properties of UWA kaolin clays used in numerical and physical modelling after Stewart (1992) and Wang and O'Loughlin (personal communication, 2022)

Property	Value (kaolin*)	Value (kaolin†)
Specific gravity, G_s	2.6	2.6
Liquid limit, LL: %	61.0	73.7
Plastic limit, PL: %	27.0	44.4
Slope of NCL, λ	0.205	0.435
Slope of URL, κ	0.044	0.044
Permeability, k_s : m/s	$\approx 1.19 \times 10^{-9}$	$\approx 1.10 \times 10^{-8}$

*Ring test numerical modelling.

†Ring test physical modelling.

experiments referred to as ‘remoulded’ tests hereafter, kaolin clay and calcareous silt were thoroughly hand remoulded, removing any effects of overconsolidation and inter-particle soil structure present. As the strength of the ‘remoulded’ samples is significantly less than that of the ‘intact’ samples, the target vertical load in ‘remoulded’ ring tests was also reduced to half of the 100 N value targeted in the ‘intact’ tests. It was assumed that any voids created in these samples due to hand remoulding will disappear during the consolidation under the target vertical load before the start of the rotation stage.

The non-dimensional interpretation of the excess pore pressure dissipation response measured by the PPTs located at the ring invert during the dissipation/consolidation stage of the ring test allowed derivation of the coefficient of consolidation. Values of c_v of $8 \text{ m}^2/\text{year}$ and $5 \text{ m}^2/\text{year}$ for kaolin clay and $7 \text{ m}^2/\text{year}$ and $2 \text{ m}^2/\text{year}$ for the calcareous silt were obtained from ‘intact’ and ‘remoulded’ tests, respectively.

Total and effective stress interpretations of frictional response

Figures 6 and 7 present the total stress and effective stress interpretations of the rotation stage of the ‘intact’ test in

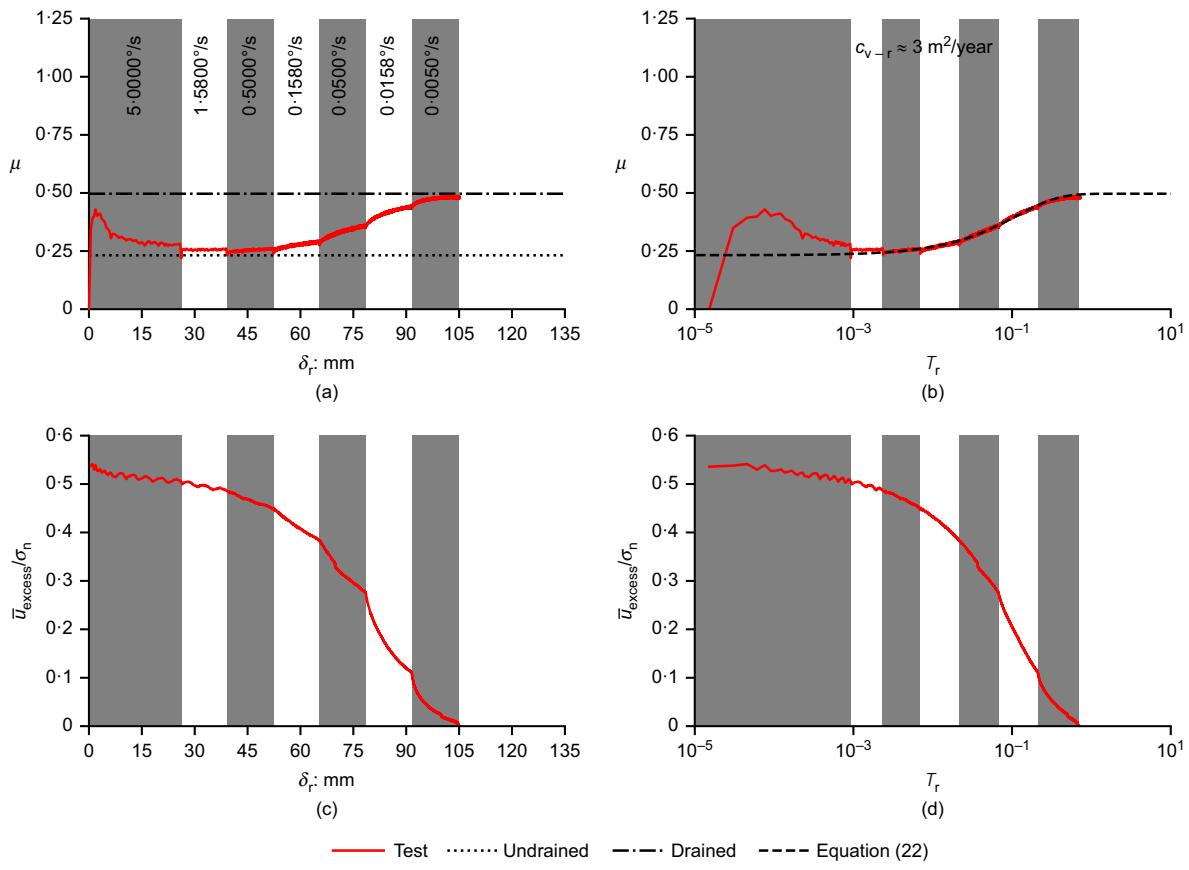


Fig. 6. Interpreted total stress friction measurements in 'intact' ring test in kaolin clay: (a) interface friction with effective displacement; (b) interface friction with dimensionless time; (c) normalised excess pore pressure with effective displacement; and (d) normalised excess pore pressure with dimensionless time

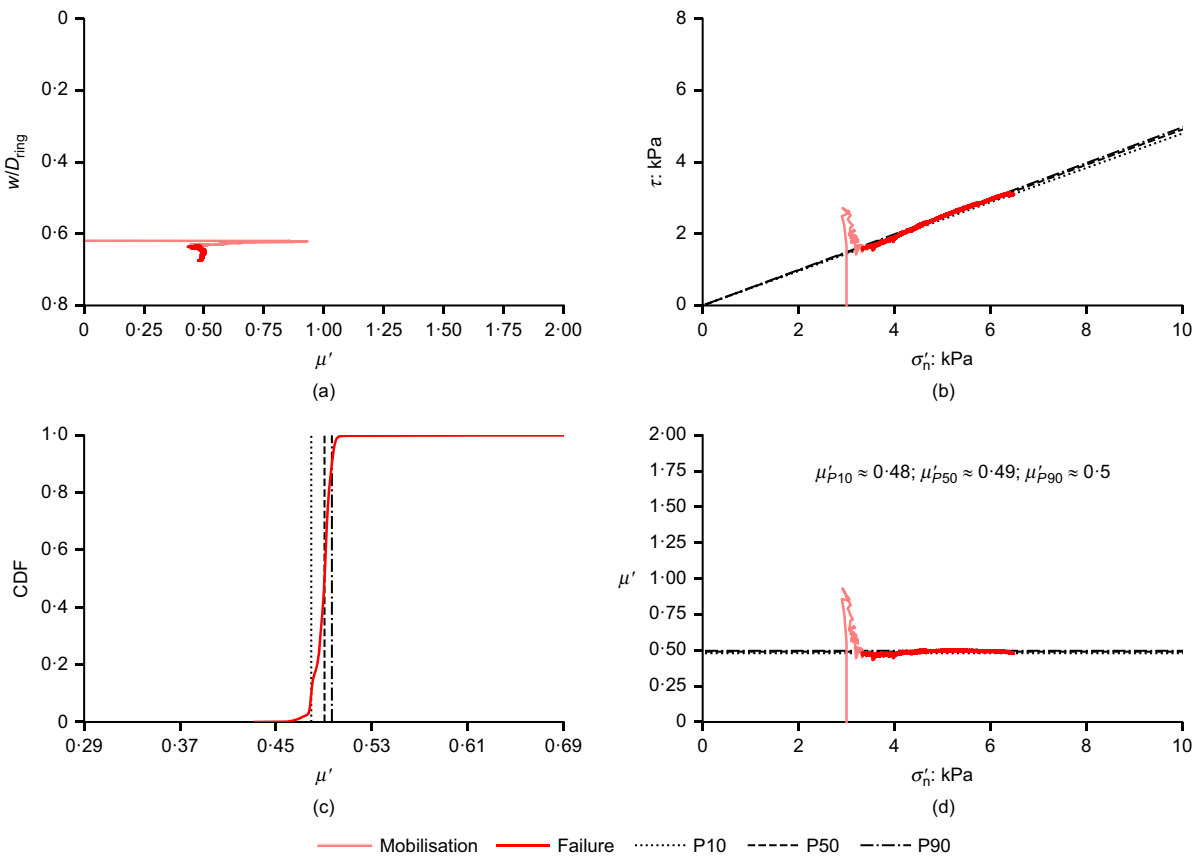


Fig. 7. Interpreted friction measurements in 'intact' ring test in kaolin clay: (a) effective friction plotted against embedment; (b) effective stress envelope; (c) cumulative density function (CDF) of effective friction; and (d) effective interface friction plotted against effective normal stress

kaolin clay. The interface friction factor μ and the average excess pore pressure normalised by total normal stress, $\bar{u}_{\text{excess}}/\sigma_n$ are plotted against rotational displacement of ring, δ_r , and dimensionless rotational time, T_r . The initial part of the measured pore pressure response has been corrected following the back-extrapolation root-time method suggested by Sully *et al.* (1999) in order to address the time lag associated with the PPT response at very fast rotation rate, as suggested by Schneider *et al.* (2020b).

As shown in Fig. 6(a), the interface friction factor μ reaches an initial peak value of 0.43 before decreasing to a value of 0.28 as a result of strain softening during the initial ring rotation with a speed of 5°/s. In the subsequent rotation stage of 1.58°/s, the friction factor reduces further to 0.26 but remained approximately constant throughout the rotation phase. The decrease in the frictional resistance due to a 0.5 log-cycle reduction in the rotation rate shows a strain-rate dependency of approximately 15% per log-cycle. Any further reduction in rotation rates (i.e. the rate segments of 0.5–0.005°/s in Fig. 6) results in an immediate drop in resistance but increases throughout the rotation phase due to partial dissipation of the pore pressure (see Figs 6(a) and 6(b)). The effect of drainage can also be seen from the pore pressure dissipation curves given in Figs 6(c) and 6(d). Partially drained conditions appear to dominate from a rotational displacement value δ_r greater than 38 mm (or $T_r = 0.0023$, or rotation speeds $\leq 0.5^{\circ}/\text{s}$). Fully drained conditions prevail at a rotational displacement value of about 105 mm (or $T_r = 0.71$), which is in line with the observation from Schneider *et al.* (2020b). The total stress-based frictional response against T_r illustrated in Fig. 6(b) has been fitted to a consolidation backbone curve using equation (22). In a multi-rate experiment, it is difficult to fit the entire frictional response using equation (24) (which represents peak undrained strength in Fig. 4(c)) due to the initial peaky response combined with the strain softening and consolidation at larger device rotation time. Therefore, equation (22) was used and a μ_u value of 0.24 was inferred from the end of the stage for the rate of 0.5°/s. The strain-rate effects are defined later, separately, based on the changes in resistance at the speed transitions. A summary of the fitting parameters adopted is given in Table 4.

Figure 7 shows the effective stress interpretations of the rotation stage of the ‘intact’ test in kaolin clay. The effective interface friction factor μ' with normalised device embedment w/D_{ring} , effective stress envelope τ with σ'_n , cumulative density function (CDF) of μ' and effective interface friction against effective normal stress are plotted in Figs 7(a), 7(b), 7(c) and 7(d), respectively. As shown in Fig. 7(a), the device settlement during the rotation w is about $0.05D_{\text{ring}}$, ensuring that the friction mobilised on the outer and inner smooth sides of the ring device was minimised. A very consistent effective stress envelope in both mobilisation (see the faded portion of the solid (red) line in Figs 7(b) and 7(c)) and failure states (see the dark portion of the solid (red) line in Figs 7(b) and 7(c)) is obtained. It can also be seen that a very tight CDF distribution of the effective friction factor μ' is obtained, with a ratio between the P_{90} and P_{10} values of μ' of only 1.04 ($\mu'_{10} \approx 0.48$, $\mu'_{50} \approx 0.49$ and $\mu'_{90} \approx 0.50$).

Figures 8 and 9 illustrate the total and effective stress derived frictional response obtained from the ‘remoulded’ test in a hand remoulded sample of the kaolin clay. The factor μ remains constant with δ_r for the fastest (undrained) rate of 5°/s due to the soil being previously hand remoulded, achieving a steady value of 0.44 in comparison to the different peak and remoulded values of μ obtained in the ‘intact’ (compare Fig. 8(a) with Fig. 6(a)). A value of 0.52 is obtained for the drained friction factor μ_d , which is close to the value of 0.51 in the ‘intact’ test. The change in rotation rate as shown in Figs 8(a) and 8(b), similar to the ‘intact’ test,

Table 4. Summary of the model fitting parameters from the ring experiments in kaolin clay and calcareous silt

Parameter	Kaolin clay		Calcareous silt	
	Intact	Remoulded	Intact	Remoulded
T_{50}	0.06	0.06	0.06	0.06
m	1.0	1.0	1.0	1.0
$T_{r,50}$	0.07	0.07	0.1	0.1
n	0.8	0.8	0.7	0.7
$\mu_{u-\text{peak}}$	0.43	0.45	1.14	1.0
μ_u	0.24	0.44	0.50	0.64
μ_d	0.51	0.52	0.76	0.81
$c_v: \text{m}^2/\text{year}$	8	5	7	2

leads to a decrease in frictional resistance in the undrained regime (i.e. $\delta_r \leq 65$ mm or $T_r \leq 0.012$), demonstrating a frictional strain-rate dependency. The effective stress interpretation of the results, as presented in Fig. 9, shows minimal device settlement during rotation, a clean and stable effective stress envelope and a CDF distribution of the effective friction with a standard deviation of $\mu'_{10} \approx 0.51$, $\mu'_{50} \approx 0.52$ and $\mu'_{90} \approx 0.53$. The effective stress envelope does not show a peak value of shear stress τ ; as high as in the ‘intact’ test due to the hand-remoulding of the soil in place of reconstitution and consolidation.

Figures 10 and 11 present the total stress interpretation of frictional response obtained from the ‘intact’ and ‘remoulded’ test in intact and hand-remoulded samples of the calcareous silt. In the ‘intact’ test, the friction factor, μ , achieves an initial peak value of 1.14 before decreasing to a value of 0.66 as a result of strain softening during the initial ring rotation with a speed of 5°/s (see Figs 10(a) and 10(b)). As the rotation speed is reduced to 1.58°/s, the factor instantaneously drops to a value of 0.59 and, in contrast to the kaolin clay response, it then continues to decrease at a constant rate due to further strain softening, indicating that larger device rotation than 30° is required to reach a fully remoulded state in an intact calcareous silt sample. The response is then dominated by partial dissipation of excess pore pressure for slower rates (i.e. 0.5–0.005°/s), leading to fully drained conditions effective at δ_r of 103 mm with a μ value of 0.76. Similarly to the ‘intact’ test, the friction factor, μ , in the ‘remoulded’ test in calcareous silt obtains a high value of 1.0 and then reduces due to strain softening, indicating the effect of the presence of stronger inter-particle fabric in calcareous silt than in kaolin clay after hand-remoulding (compare Figs 11 and 8). The μ value decreases from 0.75 to a steady value of 0.64 when the rotation speed is reduced to 1.58°/s (see Figs 11(a) and 11(b)), which indicates the complete remoulding of the interface soil fabric. The drained value of friction factor, μ_d , is 0.81, which is higher than the value of 0.76 obtained in the ‘intact’ test. A comparison of normalised excess pore pressure response during the rotation stage in the ‘intact’ and ‘remoulded’ tests (Figs 10(c), 10(d) and 11(c), 11(d)) shows that higher excess pore pressure is generated due to shearing in the ‘intact’ test than in the ‘remoulded’ test. The reason behind this is that the intact calcareous silt has higher sensitivity (i.e. presence of both intact soil structure and fabric) than the remoulded silt in which the hand-remoulding causes breakdown of the intact soil structure and fabric (although consolidation induces partial recovery of the fabric-driven sensitivity). A summary of the fitting parameters adopted for the ‘intact’ and ‘remoulded’ test data in Figs 10 and 11 is given in Table 4. For the sake of brevity, the results of effective stress interpretations of the tests in the calcareous silt are provided as online supplementary material.

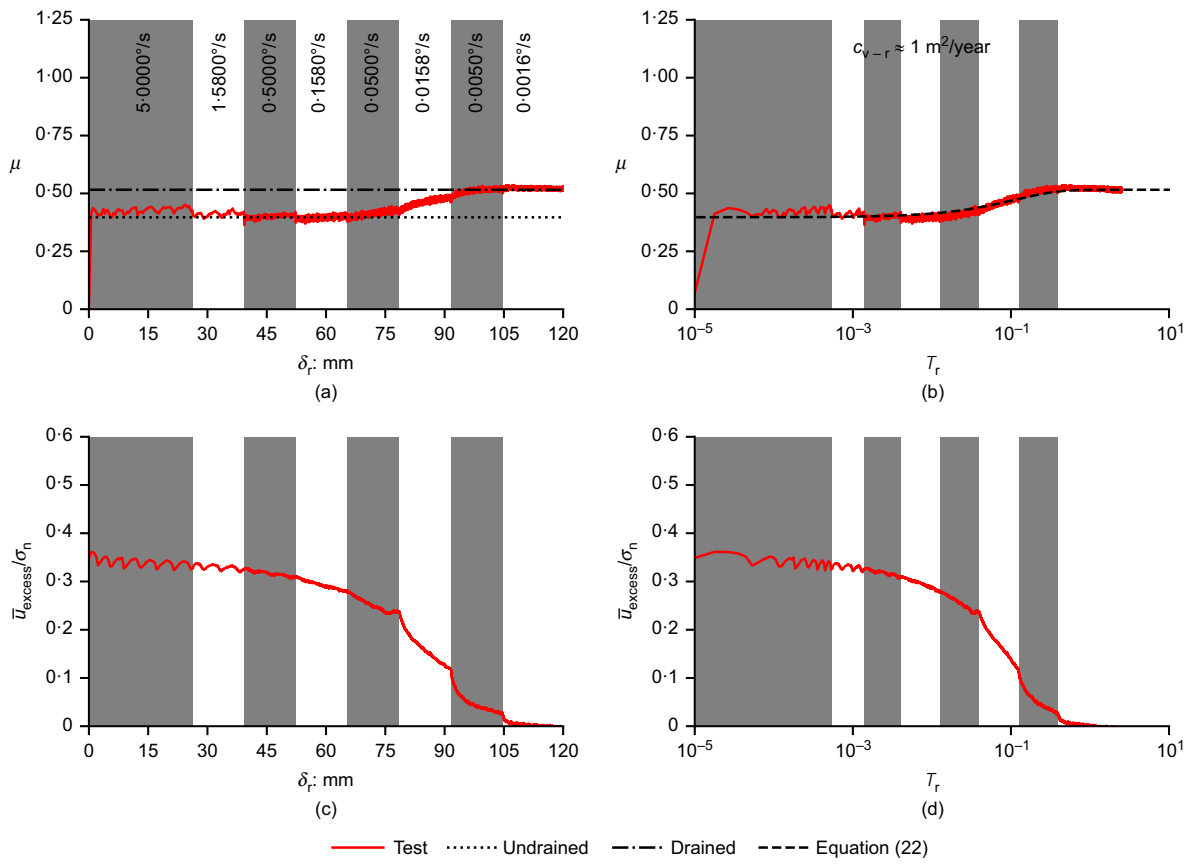


Fig. 8. Interpreted total stress friction measurements in ‘remoulded’ ring test in kaolin clay: (a) interface friction with effective displacement; (b) interface friction with dimensionless time; (c) normalised excess pore pressure with effective displacement; and (d) normalised excess pore pressure with dimensionless time

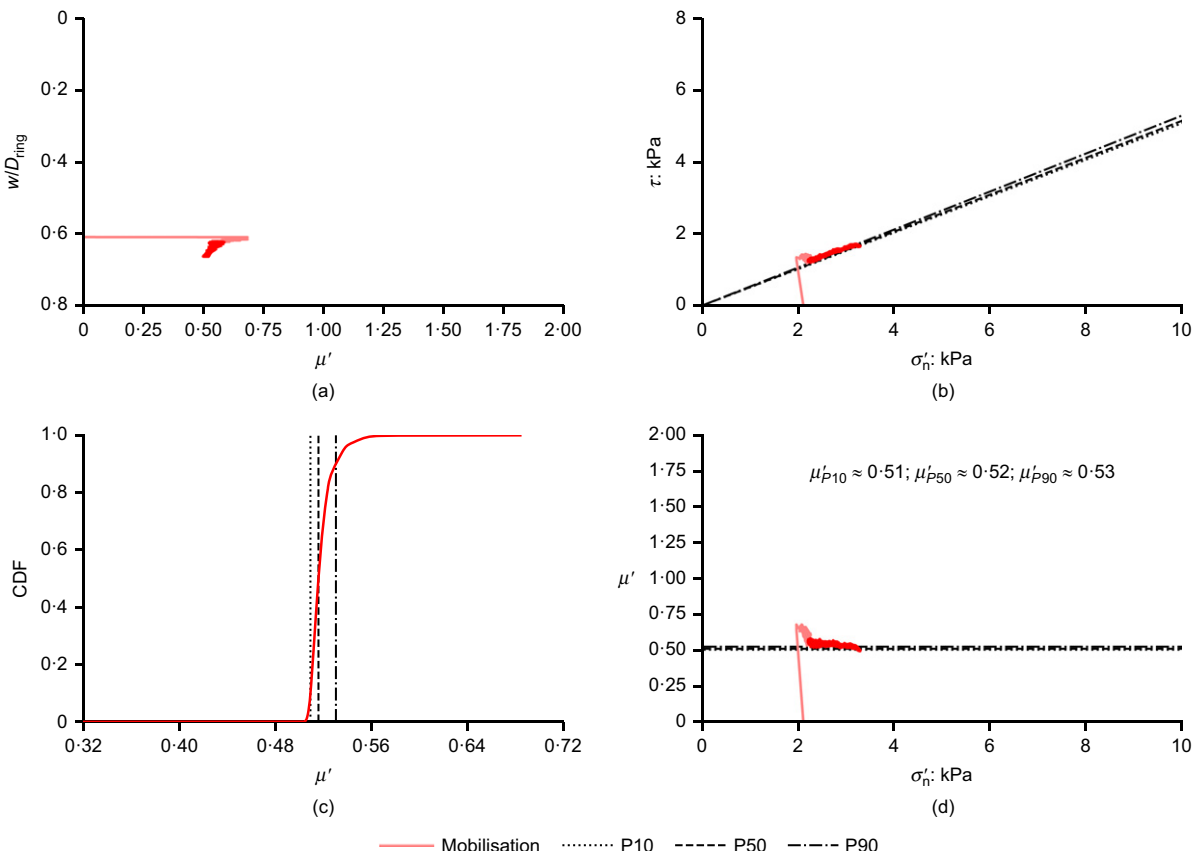


Fig. 9. Interpreted friction measurements in ‘remoulded’ ring test in kaolin clay: (a) effective friction plotted against embedment; (b) effective stress envelope; (c) CDF of effective friction; and (d) effective interface friction plotted against effective normal stress

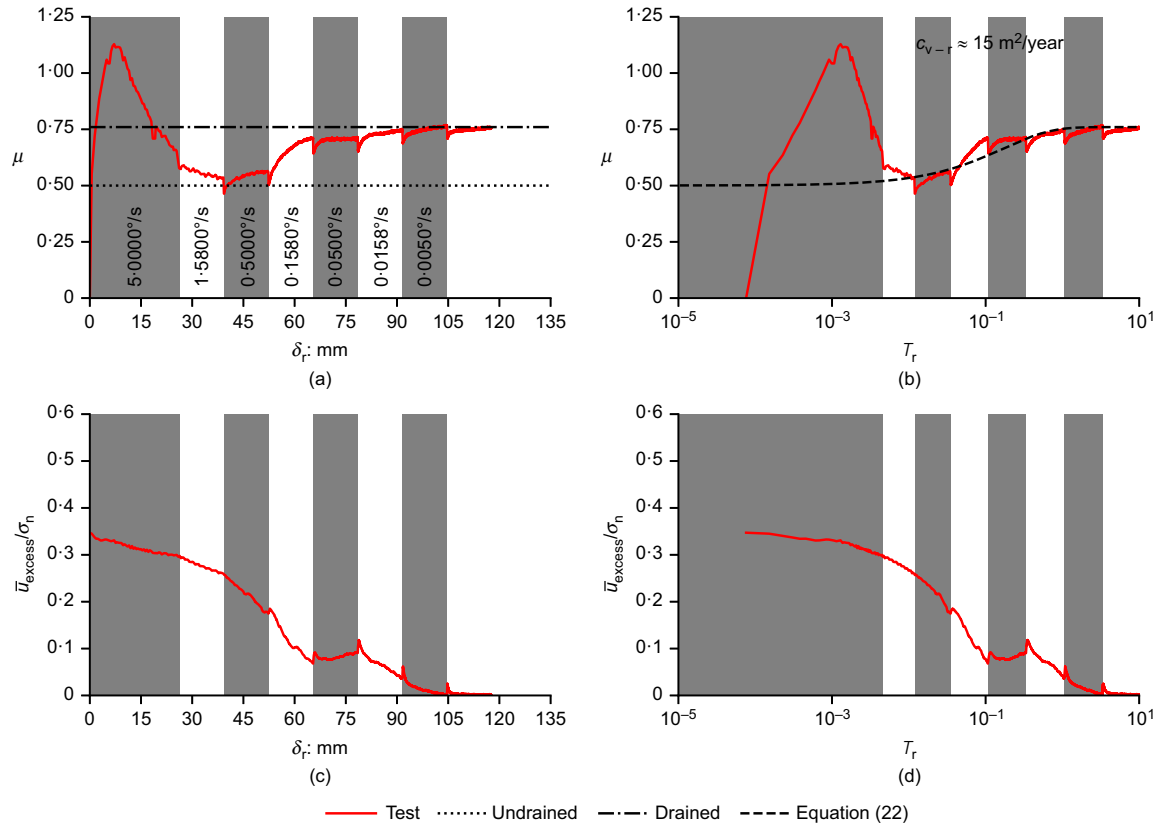


Fig. 10. Interpreted total stress friction measurements in 'intact' ring test in calcareous silt: (a) interface friction with effective displacement; (b) interface friction with dimensionless time; (c) normalised excess pore pressure with effective displacement; and (d) normalised excess pore pressure with dimensionless time

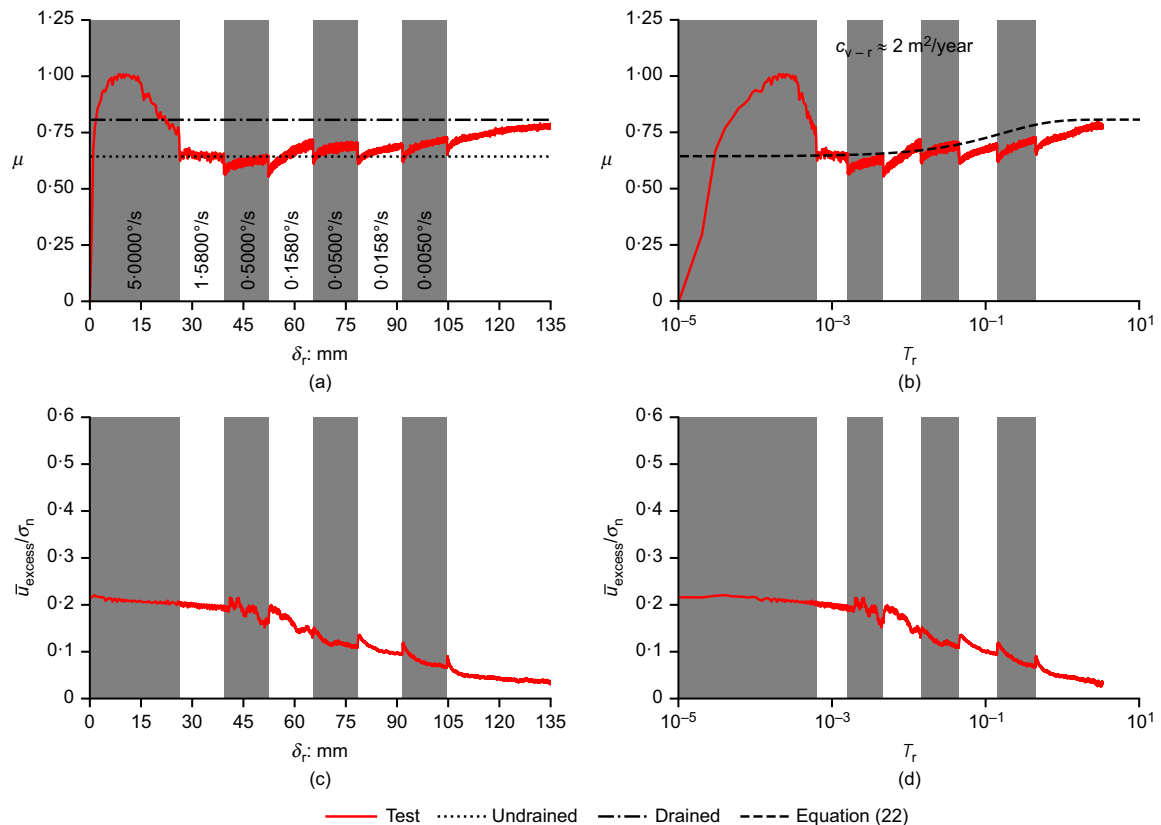


Fig. 11. Interpreted total stress friction measurements in 'remoulded' ring test in calcareous silt: (a) interface friction with effective displacement; (b) interface friction with dimensionless time; (c) normalised excess pore pressure with effective displacement; and (d) normalised excess pore pressure with dimensionless time

Interpreted $\mu - v_r D_{ring}/c_v$ backbone response

The interpreted ring interface friction responses against normalised rotation velocity $v_r D_{ring}/c_v$ extracted from the 'Intact' and 'Remoulded' tests in kaolin clay and a calcareous silt are presented in Fig. 12. Spot values of the friction factor μ were extracted for the $v_r D_{ring}/c_v$ considered in the tests from the data presented in Figs 6 and 8 for the kaolin clay and in Figs 10 and 11 for the calcareous silt. The μ values at the beginning and end of every rotation rate segment were extracted and indicated with error bars due to the difficulty associated with relating a particular velocity to increasing μ due to partial drainage (see the responses for δ_r between 45 and 90 mm in Figs 6(a) and 8(a)). For the fastest velocity, μ is taken at the end of the rotation when the interface has fully mobilised a residual state. The experimental data have been fitted using the $\mu - v_r D_{ring}/c_v$ model equation (25), capturing both consolidation and viscous effects. The values of the fitting parameters are listed in Table 5. The undrained friction value μ_u and reference nominal strain rate $(v_r/D_{ring})_{ref}$, which has been calculated from V'_{ref} , are taken at the transition from the undrained to the partially drained regime in Fig. 12. For any geotechnical site characterisation, values of the parameters controlling consolidation and strain-rate effects (i.e. V'_{50} , λ_1 , λ_2 and λ_3) can be identified from a single multi-rate ring rotation test, allowing application of the model equations in design. The limitation of the resulting curve fit is that it is only strictly representative of the friction factors mobilised from an initial state where zero consolidation has occurred at time, $t = 0$. In other words, the

device rotation time in the ring tests to mobilise the friction factors in the undrained velocity regime was very small and negligible to kick in any pore pressure dissipation before their mobilisation; therefore, the fit does not capture the influence of any potential partial drainage, which can occur with continuous rotation of the device even when the device rotation speed is sufficient to ensure undrained conditions. Any consolidation-induced hardening induced at time $t > 0$ would result in the undrained right-hand portion of the curve fit being slightly higher, but with the same magnitude of rate effect per log cycle of additional rate.

COMPARISON OF STRAIN-RATE EFFECTS FROM RING AND T-BAR TWITCH TESTS

Conventionally, strain-rate effects on undrained shear strength have been derived from element tests (e.g. Vaid & Campanella, 1977; Rangeard *et al.*, 2002) or T-bar twitch penetration tests in soft sediments (e.g. Chung *et al.*, 2006; Chow *et al.*, 2020). Therefore, T-bar twitch penetration tests were performed in kaolin clay and calcareous silt in order to provide a comparison between the rate-dependency derived in undrained friction and undrained shear resistance obtained from the ring and T-bar twitch tests, respectively. Figs 13 and 14 present the T-bar penetration resistance q_{pen} against depth z for varying penetration rates in kaolin clay and the calcareous silt. A decrease in penetration rate leads to a reduction in penetration resistance q_{pen} due to strain-rate effects as described earlier in the text. Fig. 15 summarises the

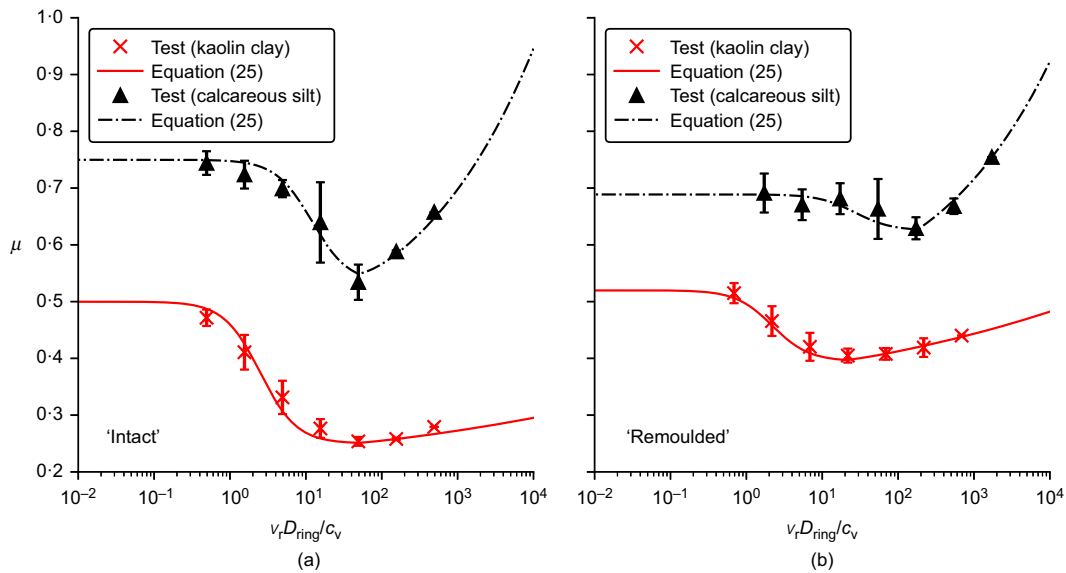


Fig. 12. Interpreted interface friction backbone curve for kaolin clay and calcareous silt derived from: (a) 'intact' ring test; and (b) 'remoulded' ring test

Table 5. Summary of the backbone model parameters in Fig. 12

Parameter	Kaolin clay		Calcareous silt	
	Intact	Remoulded	Intact	Remoulded
μ_u	0.25	0.40	0.53	0.63
μ_d	0.50	0.52	0.75	0.69
λ_1	1.8	1.8	1.8	1.8
λ_2	0.35	0.35	0.35	0.35
λ_3	0.10	0.10	0.26	0.26
V'_{ref}	50	21	49	181
$(v_r/D_{ring})_{ref}: s^{-1}$	0.0178	0.0053	0.0174	0.0183
V'_{50}	2.5	2.2	12	27

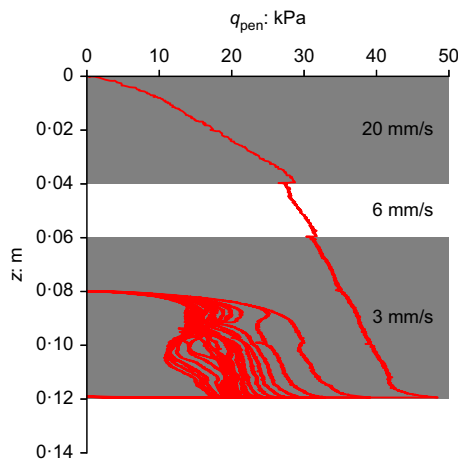


Fig. 13. 'Intact' T-bar twitch penetration resistance measurements in kaolin clay

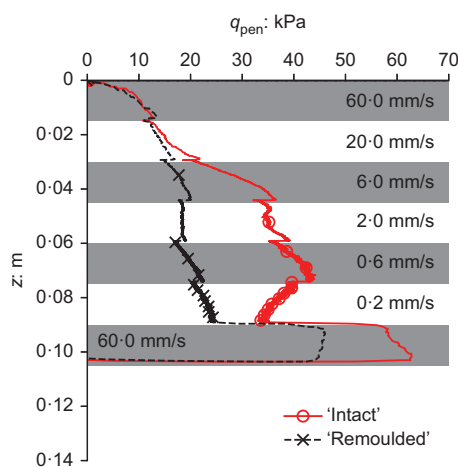


Fig. 14. 'Intact' and 'remoulded' T-bar twitch penetration resistance measurements in calcareous silt

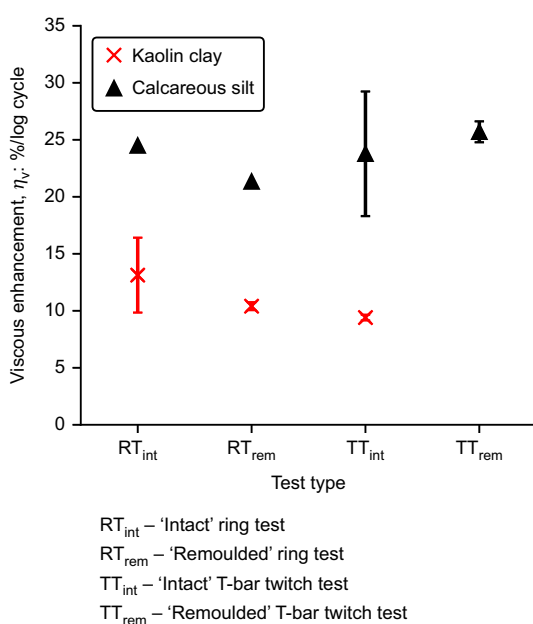


Fig. 15. Viscous enhancement of strength and friction in kaolin clay and calcareous silt obtained from ring and T-bar tests

strain-rate effect on q_{pen} extracted for the rate changes for penetration rates equal to or greater than 2 mm/s observed in Figs 13 and 14 alongside similar measurements derived from the ring tests. The results are presented in the form of a mean with error bars where more than one rate change was performed in undrained conditions in either the ring or T-bar tests. It can be seen that the strain-rate dependency obtained using the ring tests and T-bar tests are in close agreement, with viscous enhancement η_v of 9–16% /log cycle and 18–29% /log cycle for kaolin clay and calcareous silt, respectively. This was expected since the soil-ring interface comprised bonded coarse silica sand, which causes the soil immediately beneath the ring to fail in shear as opposed to causing soil-ring interface slippage. The largest error is associated with the η_v value obtained from the 'intact' T-bar twitch test in calcareous silt; it has an error bound of 18–29% /log cycle, compared with the range of η_v values of 22–26% /log cycle obtained from the other tests in calcareous silt. This shows that measurement of rate-dependency using the ring penetrometer can be achieved with a precision similar to that achievable with a miniature T-bar twitch test.

CONCLUSIONS

This paper has presented the numerical and physical modelling of a shallow penetrometer device used to characterise shallow seabed sediments. The focus of this paper was on measuring the strain-rate dependency, strain-softening and consolidation properties of soft sediments. The numerical model of the ring penetrometer test comprised penetration, dissipation and rotation phases, simulated using SMCC and VRS constitutive models in a sequential LDPE analysis. The numerical results were then used in interpretation of the measurements of the consolidation and interface frictional properties of the two different soil types (i.e. kaolin clay and calcareous silt). The main highlights of the results obtained using numerical and physical modelling techniques are summarised as follows.

- (a) The numerical analyses facilitated the derivation of simple conceptual models that can be used to describe the variation of interface friction with both sliding rate and time.
- (b) The analyses suggested that the ring penetrometer could potentially be used to measure the strain-rate dependency of the interface friction at low stresses in addition to the consolidation and strain-softening characteristics.
- (c) The ring penetrometer experiments performed in both intact and remoulded specimens produced data that facilitated very consistent interpretation of the consolidation and frictional properties. For example, the values of the coefficient of consolidation c_v , which are difficult to get within a factor of 10 in reality (Stanier & White, 2015), obtained from the 'intact' and 'remoulded' tests in kaolin clay are 8 and 5 m^2/year , respectively.
- (d) Almost all of the typical geotechnical design parameters related to shallow seabed characterisation (c_v , μ , μ' or δ , η_v) can be obtained from a single multi-rate ring penetrometer experiment.
- (e) The strain-rate-induced enhancement of undrained friction and shear resistance were measured as 9–16% /log cycle and 18–29% /log cycle in kaolin clay and calcareous silt, respectively.
- (f) The strain-rate dependency of the interface friction obtained from the ring penetrometer tests agrees well

with those derived by more conventional means, such as by using miniature T-bar twitch penetration tests.

ACKNOWLEDGEMENTS

The first author is supported by a University of Western Australia Scholarship for International Research Fees, University Postgraduate Award and ad hoc top-up scholarship. Prior to moving to the University of Cambridge, the third author was supported at the University of Western Australia by an ARC DECRA Fellowship (DE170100119).

NOTATION

A	parameter controlling relative contribution of plastic volumetric and plastic shear strains in softening
A_c	penetrometer–soil contact surface area
c_v	vertical coefficient of consolidation
c_{v-r}	c_v value in rotation stage of ring test
D	T-bar diameter
D_{ring}	ring cross-section width
e	void ratio
\dot{e}	rate of void ratio evolution
F	equivalent axial force
f	shape of static yield surface
f_d	shape of dynamic yield surface
G	shear modulus
K	bulk modulus of soil
k	sensitivity degradation rate
M	critical state line gradient
m	fitting parameter
N^*	intercept of the normal compression line at $p' = 1$ kPa
N_v	viscosity exponent
n	fitting parameter
p'	mean effective stress
p_c	size of reference/static yield surface for $s_{epi} = 1$
p_{cd}	size of dynamic loading surface passing through the current stress state
p_{cs}	size of reference/static yield surface for $s_{ep} > 1$, equal to $s_{ep}p_c$
p_r	reference pressure
q	deviatoric stress
q_{pen}	T-bar penetration resistance
R	sensitivity recovery parameter
R_a	arithmetic average roughness
r_{eff}	ring lever arm
S_f	final soil sensitivity on complete remoulding (typically taken as 1)
S_t	true soil sensitivity
s_{ep}	current value of sensitivity state variable
\dot{s}_{ep}	rate of s_{ep} evolution
s_{epf}	final value of s_{ep}
s_{epi}	initial value of s_{ep}
s_u	undrained soil shear strength
s_{ui}	intact s_u
T	dimensionless dissipation time, $c_v t / D_{ring}^2$
T_{50}	dimensionless time for 50% excess pore pressure dissipation
T_r	dimensionless time, $c_v t_r / D_{ring}^2$
$T_{r,50}$	T_r value required for achieving μ value halfway between μ_u and μ_d
T_{res}	torsional resistance
t	dissipation time
t_{50}	time required for 50% excess pore pressure dissipation
t_r	rotation time
u_{excess}	excess pore pressure at an invert point
$u_{excess-i}$	initial value of u_{excess} at an invert point
\bar{u}_{excess}	average invert excess pore pressure
$\bar{u}_{excess-i}$	initial value of \bar{u}_{excess}
V	vertical load/resistance
V'	dimensionless rotational velocity, $v_r D_{ring} / c_v$
V_{max}	V' value at target penetration
V'_{50}	V' at which μ is halfway between μ_u and μ_d limits
V'_{ref}	reference value of V' , where transition of undrained to partially drained regime occurs
v_p	penetration rate
v_r	rotation speed
w	ring penetration depth
z	T-bar penetration depth
β	pore pressure scaling parameter
γ_w	unit weight of water
δ	effective friction angle of soil
δ_r	linear displacement of ring in rotation stage
δ_{rp}	δ_r required to mobilise μ_u
$\dot{\varepsilon}_g^p$	plastic deviatoric strain rate
$\dot{\varepsilon}_s$	equivalent plastic strain rate
$\dot{\varepsilon}_v$	volumetric strain rate
$\dot{\varepsilon}_v^p$	plastic volumetric strain rate
$\dot{\varepsilon}^{vp}$	viscoplastic strain rate
η	strain-rate effect on interface friction factor
η_v	viscous enhancement of interface friction or shear strength
κ^*	slope of the unload–reload line in $\ln(1+e)$ – $\ln p'$ space
λ^*	slope of the normal compression line in $\ln(1+e)$ – $\ln p'$ space
λ_1	fitting parameter
λ_2	viscous property of soil
λ_3	shear thinning index
μ	interface friction factor based on total stress interpretation
μ'	interface friction factor based on effective stress interpretation
μ_d	drained interface friction factor
$\mu_{P_{10}}$	P_{10} value of μ'
$\mu_{P_{50}}$	P_{50} value of μ'
$\mu_{P_{90}}$	P_{90} value of μ'
μ_u	undrained interface friction factor
μ_{u-peak}	peak undrained interface friction factor
μ_v	fluidity parameter
ν	Poisson's ratio
σ_n	average normal pressure or stress
σ'_n	average effective normal pressure or stress
τ	interface shear stress
τ_u	undrained interface shear stress
$\phi(F)$	overstress function
ϕ_c	critical state effective friction angle of soil

REFERENCES

- Butterfield, R. (1979). A natural compression law for soils (an advance on e -log). *Géotechnique* **29**, No. 4, 469–480, <https://doi.org/10.1680/geot.1979.29.4.469>.
- Chow, S. H., O'Loughlin, C. D., Zhou, Z., White, D. J. & Randolph, M. F. (2020). Penetrometer testing in a calcareous silt to explore changes in soil strength. *Géotechnique* **70**, No. 12, 1160–1173, <https://doi.org/10.1680/jgeot.19.P.069>.
- Chung, S. F., Randolph, M. F. & Schneider, J. A. (2006). Effect of penetration rate on penetrometer resistance in clay. *J. Geotech. Geoenviron. Engng* **132**, No. 9, 1188–1196.
- Cocjin, M. L., Gourvenec, S. M., White, D. J. & Randolph, M. F. (2014). Tolerably mobile subsea foundations – observations of performance. *Géotechnique* **64**, No. 11, 895–909, <https://doi.org/10.1680/geot.14.P.098>.
- DNV (Det Norske Veritas) (2017). *DNV-RP-F114 pipe-soil interaction for submarine pipelines. Technical report*. Oslo, Norway: DNV.
- Hu, Y. & Randolph, M. F. (1998). A practical numerical approach for large deformation problems in soil. *Int. J. Numer. Analyt. Methods Geomech.* **22**, No. 5, 327–350.
- Lehane, B. M., O'Loughlin, C. D., Gaudin, C. & Randolph, M. F. (2009). Rate effects on penetrometer resistance in kaolin. *Géotechnique* **59**, No. 1, 41–52, <https://doi.org/10.1680/geot.2007.00072>.
- Mašín, D. (2009). Comparison of predictive capabilities of selected elasto-plastic and hypoplastic models for structured clays. *Soils Found.* **49**, No. 3, 381–390.
- Meyer, V. M., Dyvik, R. & White, D. J. (2015). Direct shear interface tests for pipe-soil interaction assessment. In *Frontiers in offshore geotechnics III* (ed. V. Meyer), pp. 423–428. Leiden, the Netherlands: CRC Press/Balkema.
- Perzyna, P. (1966). Fundamental problems in viscoplasticity. In *Advances in applied mechanics* (eds G. G. Chernyi, H. L. Dryden, P. Germain, L. Howarth, W. Olszak, W. Prager,

- R. F. Probstein and H. Ziegler), vol. 9, pp. 243–377. New York, NY, USA: Academic Press.
- Randolph, M. F., White, D. J. & Yan, Y. (2012). Modelling the axial soil resistance on deep-water pipelines. *Géotechnique* **62**, No. 9, 837–846, <https://doi.org/10.1680/geot.12.OG.010>.
- Randolph, M. F., Stanier, S. A., O'Loughlin, C. D., Chow, S. H., Bienen, B., Doherty, J. P., Mohr, H., Ragni, R., Schneider, M. A., White, D. J. & Schneider, J. A. (2018). Penetrometer equipment and testing techniques for offshore design of foundations, anchors and pipelines. In *Cone penetration testing 2018*. (eds M. A. Hicks, F. Pisaniò and J. Peuchen), ch. 1, pp. 3–24. Leiden, the Netherlands: CRC Press.
- Rangéard, D., Hicher, P. Y. & Moulin, G. (2002). *Identification des caractéristiques hydro-mécaniques d'une argile par analyse inverse d'essais pressiométriques*. PhD thesis, Ecole Centrale de Nantes et l'Université de Nantes, Nantes, France (in French).
- Robinson, S. (2019). *Rate effect behaviour of different clays from high speed triaxial element testing*. PhD thesis, University of Dundee, Dundee, UK.
- Schneider, M. A., Stanier, S. A., Chatterjee, S., White, D. J. & Randolph, M. F. (2019). The parkable piezoprobe for determining c_v and strength – modelling and interpretation methods. *Géotechnique* **69**, No. 5, 458–469, <https://doi.org/10.1680/jgeot.18.P004>.
- Schneider, M. A., Stanier, S. A., White, D. J. & Randolph, M. F. (2020a). Apparatus for measuring pipe-soil interaction behavior using shallow ‘pipe-like’ penetrometers. *Geotech. Test. J.* **43**, No. 3, 622–640.
- Schneider, M. A., Stanier, S. A., White, D. J. & Randolph, M. F. (2020b). Shallow penetrometer tests: theoretical and experimental modelling of penetration and dissipation stages. *Can. Geotech. J.* **57**, No. 4, 568–579.
- Singh, V., Stanier, S., Bienen, B. & Randolph, M. F. (2021). Modelling the behaviour of sensitive clays experiencing large deformations using non-local regularisation techniques. *Comput. Geotech.* **133**, 104025.
- Singh, V., Stanier, S., Bienen, B. & Randolph, M. F. (2022). A viscoplastic recoverable sensitivity model for fine-grained soils. *Comput. Geotech.* **147**, 104725.
- Stanier, S. A. & White, D. J. (2015). Shallow penetrometer penetration resistance. *J. Geotech. Geoenviron. Engng* **141**, No. 3, 04014117.
- Stewart, D. P. (1992). *Lateral loading of piled bridge abutments due to embankment construction*. PhD thesis, The University of Western Australia, Perth, WA, Australia.
- Sully, J. P., Robertson, P. K., Campanella, R. G. & White, D. J. (1999). An approach to evaluation of field CPTU dissipation data in overconsolidated fine-grained soils. *Can. Geotech. J.* **36**, No. 2, 369–381.
- Vaid, Y. P. & Campanella, R. G. (1977). Time-dependent behavior of undisturbed clay. *J. Geotech. Engng Div.* **103**, No. 7, 693–709.
- White, D. J., Gaudin, C., Boylan, N. & Zhou, H. (2010). Interpretation of T-bar penetrometer tests at shallow embedment and in very soft soils. *Can. Geotech. J.* **47**, No. 2, 218–229.
- Yan, Y. (2013). *Novel methods for characterising pipe-soil interaction forces in situ in deep water*. PhD thesis, The University of Western Australia, Perth, WA, Australia.
- Yan, Y., White, D. J. & Randolph, M. F. (2011). Penetration resistance and stiffness factors for hemispherical and toroidal penetrometers in uniform clay. *Int. J. Geomech.* **11**, No. 4, 263–275.
- Yin, Z. Y. & Hicher, P. Y. (2008). Identifying parameters controlling soil delayed behaviour from laboratory and in situ pressuremeter testing. *Int. J. Numer. Analyt. Methods Geomech.* **32**, No. 12, 1515–1535.
- Yin, Z. Y., Hicher, P. Y., Riou, Y. & Huang, H. W. (2006). An elasto-viscoplastic model for soft clay. In *GeoShanghai 2006: soil and rock behavior and modeling* (eds R. Luna, Z. Hong, G. Ma and M. Huang), Geotechnical Special Publication 150, pp. 312–319. Reston, VA, USA: American Society of Civil Engineers.